# New Insights on Critical Transitions
# of Single-Neuron Dynamics

H. He[a,b], K. Zhang[a], H. Yan[c] and J. Wang[a,b,d,*]

[a]*State Key Laboratory of Electroanalytical Chemistry, Changchun Institute of Applied Chemistry, Chinese Academy of Sciences, Changchun, Jilin 130022, China*
[b]*School of Applied Chemistry and Engineering, University of Science and Technology of China, Hefei, Anhui 230026, China*
[c]*Center for Theoretical Interdisciplinary Sciences, Wenzhou Institute, University of Chinese Academy of Sciences, Wenzhou, Zhejiang 325001, China*
[d]*Department of Chemistry and of Physics and Astronomy, State University of New York at Stony Brook, Stony Brook, New York 11794-3400, United States*

Many theoretical models depicting excitable cells stem from the Hodgkin–Huxley model. Over the past few decades, quantitative studies on its electrophysiology and nonlinear dynamics have yielded considerable progress. In this study, we employ a landscape and flux theory to statistically explore the global dynamic characteristics of the classical Hodgkin–Huxley neuron. We quantify the underlying landscape and flux to address global stability. Our results provide an intuitive understanding of a global picture of the dynamic system. By quantifying the average curl flux, we reveal that it serves as the dynamical origin for the emergence of a new state and a dynamical indicator for bifurcation. In addition, we quantitatively calculate the entropy production, identifying it as an essential thermodynamic indicator for bifurcation. The time asymmetry of the cross-correlations can be directly computed from existing experimental time series, offering a practical indicator for bifurcation analysis. This paper presents our findings and their implications for a better understanding of the behavior of excitable cells.

topics: non-equilibrium Hodgkin–Huxley (HH) neuron dynamics, landscape, curl flux, critical transition

## 1. Introduction

The pioneering work of Hodgkin and Huxley laid the foundation for unraveling the mysteries of neuron excitability, providing a fundamental theoretical framework for investigating the electrical properties of neurons [1–6]. Since then, research in this field has expanded to explore the intricacies of neuron behavior and the mechanisms underlying neuronal activity. One aspect of this research was the investigation of local bistability, which has been extensively studied through the combined use of numerical calculations and bifurcation theory. Specifically, the condition that the direct current (DC) $I$ is the only bifurcation parameter has been explored in detail [7, 8]. In addition, the introduction of the effective calcium concentration to modify the deterministic equations allowed the exploration of bifurcation diagrams in the $[k^+]$–$V$ plane ($[k^+]$ representing both extracellular and intracellular potassium concentration [9]). Recent research has focused on the study of a two-bifurcation-parameter system [10], as well as the exploration of multiparameter bifurcation [11]. Of particular interest is the coexistence of stable quiescence and stable limit cycles localized in specific ranges of bifurcation parameters, which has led to the use of statistical methods to describe the nonlinear dynamics of Hodgkin–Huxley neurons [12, 13]. Overall, the work of Hodgkin and Huxley has paved the way for continued investigation into the complex dynamics of neurons and their underlying mechanisms [14]. Besides, the Hodgkin–Huxley (HH) model describes neurons that exhibit local bistability and undergo a subcritical Hopf bifurcation, which provides the possibility of state transitions and forms the basis for the dynamical mechanism of

bursting oscillations in neurons. One way to achieve this is by adding stochastic noise [15–18]. Biological neurons are constantly exposed to various types of noise in their environment, and considering the stochastic oscillations is necessary when studying their dynamical mechanisms. Although stochastic dynamics in the HH-model neurons have been partially studied, quantifying and understanding the physical mechanism of their global behavior to reveal the underlying phase transition mechanisms remains challenging.

In this work, we investigate the local bistable properties of the original four-dimensional Hodgkin–Huxley equations under the influence of noise. Additionally, we apply the recently developed theory of landscape and flux to reveal its stochastic dynamical mechanisms [19–21]. Given that the Hodgkin–Huxley neuron model is subject to noise, the prediction of neuron trajectories becomes partially infeasible. In such scenarios, it becomes more meaningful to quantitatively assess the statistical distribution of individual neuron states at different times and to characterize the overall distribution within the whole state space. The landscape–flux framework has been employed in non-equilibrium systems, offering valuable insights into associated behaviors [22–29]. This framework has proven to be a useful tool for gaining a deeper understanding of the dynamics and behavior of such systems. However, only a limited number of studies have used this theory to investigate the nonlinear dynamical mechanisms of individual HH neurons. Therefore, we explore state transitions using the topographical structure of the potential landscape and quantify the probabilistic flux and entropy production in the state space. By examining their relationship with the bifurcation parameters of the system, we analyze their roles and contributions in state transitions and the emergence of new states. We found that average flux and entropy production rate can serve as indicators of bifurcation. We also calculate differences in cross-correlation functions forward-in-time and backward-in-time and discuss the observed behaviors and the degree of time-reversal symmetry breaking. This provides a practical indicator for bifurcation that can be directly extracted from experimental time series. Moreover, we analyze the behavior of the critical slowing down in bifurcation by investigating the characteristic decay time of autocorrelation functions and its correlation near the bifurcation. By conducting these explorations, we enhance our comprehension of the nonlinear dynamical mechanisms exhibited by HH neuron models in the presence of noise, facilitating quantitative analysis. This research has substantial implications for illuminating the behavior of individual neurons and the overall functionality of the nervous system. Drawing upon the intricate landscape structure of its diverse states, we present a fresh perspective on this fundamental aspect of neuronal excitability.

## 2. Methods

### 2.1. Stochastic Hodgkin–Huxley equations

The Hodgkin–Huxley (HH) model has made substantial contributions to the understanding of neuronal electrophysiology, providing a foundational framework for studying the electrical properties of neurons. This model is characterized by a system of four nonlinear ordinary differential equations (ODEs). In the real world, neurons are constantly influenced by noise, including external noise (such as interference signals from the stimulus current) and internal noise (such as stochasticity in ion channels). These noises affect the activity of neurons, introducing randomness and uncertainty into the neuronal system. When investigating neuronal behavior and information processing, it is crucial to take these noise factors into account. Many previous studies introduced current noise and subunit noise to an HH neuron [30–32]. Due to ease of implementation and computational efficiency, current noise and subunit noise have become widely adopted as approximations for modeling stochastic HH dynamics. In our study, we incorporated these two types of noise into the statistical HH model, which is mathematically represented by a system of four stochastic nonlinear equations

$$C_m \frac{\mathrm{d}V}{\mathrm{d}t} = -\overline{g_{\mathrm{K}}}\, n^4 (V - V_{\mathrm{K}}) - \overline{g_{\mathrm{Na}}}\, m^3 h\, (V - V_{\mathrm{Na}})$$

$$-g_L(V - V_L) + I + \Gamma_1(\boldsymbol{x}, t),$$

$$\frac{\mathrm{d}m}{\mathrm{d}t} = \alpha_m(V)(1 - m) - \beta_m(V)m + \Gamma_2(\boldsymbol{x}, t),$$

$$\frac{\mathrm{d}h}{\mathrm{d}t} = \alpha_h(V)(1 - h) - \beta_h(V)h + \Gamma_3(\boldsymbol{x}, t),$$

$$\frac{\mathrm{d}n}{\mathrm{d}t} = \alpha_n(V)(1 - n) - \beta_n(V)n + \Gamma_4(\boldsymbol{x}, t). \tag{1}$$

Here, $\Gamma_1(\boldsymbol{x}, t) = A_V \Gamma(\boldsymbol{x}, t)$, $\Gamma_2(\boldsymbol{x}, t) = A_m \Gamma(\boldsymbol{x}, t)$, $\Gamma_3(\boldsymbol{x}, t) = A_h \Gamma(\boldsymbol{x}, t)$, $\Gamma_4(\boldsymbol{x}, t) = A_n \Gamma(\boldsymbol{x}, t)$, $\boldsymbol{A}_{\Gamma(\boldsymbol{x}, t)} = [A_V, A_m, A_h, A_n]$ is the scaling factors matrix of Gaussian white noise, while $\Gamma$ represents Gaussian white noise, which is a type of stochastic force. In this article, we transformed the third equation of (1) by multiplying both sides of it by 100, obtaining the final form $\frac{\mathrm{d}h1}{\mathrm{d}t} = \alpha_h(V)(100 - h1) - \beta_h(V)h1 + \Gamma_3(\boldsymbol{x}, t)$ (where $h1 = 100h$). In (1), $V$ is the membrane potential, and $I$ is defined as $I = I_{\mathrm{stim}}/A$, denoting the stimulus current applied per unit area of the cell membrane. The scaling factor for potassium ion conductance, measured in $\mathrm{mS/cm}^2$, is $\overline{g_{\mathrm{K}}}$. The variable $n$ is designated as the activation variable for potassium ($\mathrm{K}^+$) channels, ranging from 0 to 1. This reflects the probability of each subunit in the channel being open. The model assumes that a potassium channel consists of four cooperative subunits, fully open only when all are activated. This assumption is an effective

simplification that proves to be very effective in many scenarios. The equilibrium potential of potassium ions is represented by $V_{\mathrm{K}}$. Then, the term $\overline{g_{\mathrm{K}}}\, n^4(V-V_{\mathrm{K}})$ naturally depicts the current across the cell membrane caused by potassium ions. Accordingly, $\overline{g_{\mathrm{Na}}}$ is the scaling factor for sodium ion conductance. The gating variables $m$ and $h$ are dimensionless and represent the activation variable and the inactivation variable for sodium channels, respectively. They also range from 0 to 1 and jointly represent the opening and inactivation of sodium channels, a concept validated by further research. The equilibrium potential of sodium ions is represented by $V_{\mathrm{Na}}$, and $\overline{g_{\mathrm{Na}}}\, m^3 h(V-V_{\mathrm{Na}})$ is the component of the current across the cell membrane caused by sodium ions. Moreover, the term $g_L(V-V_L)$ denotes additional factors influencing the generation of positive or negative currents across the cell membrane, where $g_L$ is the leak conductance — a constant signifying the total conductance of other ions across the membrane, and $V_L$ is the equilibrium potential for the leak current, generally approximating the resting membrane potential. The capacitance of the neuronal membrane is represented by $C_m$.

In the above system of nonlinear ODEs, the quantitative description of $\alpha_x$ and $\beta_x$, where $x$ can represent $m$, $h$, or $n$, takes the form

$$\alpha_m = \frac{\overline{\alpha_m}\,(V-vm)}{1 - \mathrm{e}^{-(V-vm)/K_{\alpha m}}},$$

$$\beta_m = \overline{\beta_m}\, \mathrm{e}^{-V/K_{\beta m}},$$

$$\alpha_h = \overline{\alpha_h}\, \mathrm{e}^{-V/K_{\alpha h}},$$

$$\beta_h = \frac{\overline{\beta_h}}{1 + \mathrm{e}^{-(V-vh)/K_{\beta h}}},$$

$$\alpha_n = \frac{\overline{\alpha_n}\,(V-vn)}{1 - \mathrm{e}^{-(V-vn)/K_{\alpha n}}}, \beta_n = \overline{\beta_n}\, \mathrm{e}^{-V/K_{\beta n}}. \qquad (2)$$

In (1)–(2), $\alpha_m$ and $\beta_m$ represent the rates at which activation of molecules opens or closes sodium ion channels, respectively. The scaling factors for these rates are denoted as $\overline{\alpha_m}$ and $\overline{\beta_m}$. The equilibrium potentials for activation and inactivation processes in sodium channels are represented by $vm$ and $vh$, respectively. Similarly, $\alpha_h$ and $\beta_h$ denote the rates at which inactivating molecules switch between open and closed states in sodium channels, with associated constants $\overline{\alpha_h}$ and $\overline{\beta_h}$. For potassium ion channels, $\alpha_n$ and $\beta_n$ describe the rates of subunit gate transitions, with $vn$ indicating their equilibrium potential. The constants related to these rates and transitions in both sodium and potassium channels are $K_{\alpha m}$, $K_{\beta m}$, $K_{\alpha h}$, $K_{\beta h}$, $K_{\alpha n}$, and $K_{\beta n}$. These parameters collectively define the gating kinetics of the ion channels in the model.

Focusing on the sodium and potassium ion channel dynamics in neurons, the HH model accurately simulates Na$^+$ and K$^+$ ion flows during action potentials and response to stimulus variations, elucidating action potential frequency modulation. The HH model quantitatively explains action potential generation and phenomena such as refractory periods and anode break effects. Although the HH model provides an idealized representation of neuronal electrophysiological activity, and HH-like models based on ion channels can capture various aspects of neuronal characteristics, it is evident that each neural system operates as a non-equilibrium system that is constantly influenced by input and stochastic disturbances. These random noise sources, originating from the environment and inherent system dynamics, play a crucial role in neurophysiology [33, 34]. Therefore, analyzing stochastic dynamic phenomena in neuronal models holds the utmost significance. In our investigation, we augment the original system of nonlinear ODEs by adding Gaussian white noise terms, resulting in a series of Langevin equations (LEs) [15].

## 2.2. Landscape and flux theory

When a biological system is functioning, it is inevitably subjected to intrinsic noise, which is inherent to any system operating above absolute zero temperature. There are also external fluctuations arising from the environment. To simplify our analysis, we use Gaussian white noise as a means of simulating environmental effects. Consequently, the inclusion of noise modifies the dynamics described by $\frac{d\boldsymbol{x}}{dt} = \boldsymbol{F}(\boldsymbol{x}) + \Gamma(\boldsymbol{x},t)$, where $\Gamma(\boldsymbol{x},t)$ is Gaussian white noise. Here, $\boldsymbol{F}(\boldsymbol{x})$ represents the driving force of the system, which corresponds to the deterministic HH equations described in (9) in the Appendix. The vector variable $\boldsymbol{x}$ represents the state of the studied neuron in the phase space, specifically characterized by $(V, m, h, n)$. The amplitude of the noise can be determined by $\langle \Gamma(\boldsymbol{x},t)\Gamma(\boldsymbol{x},t') \rangle = 2D(\boldsymbol{x})\,\delta(t-t') = 2\mathcal{D}\,G(\boldsymbol{x})\,\delta(t-t')$, where $\mathcal{D}$ is the intensity of the noise and $G(\boldsymbol{x})$ is a diffusion matrix. Deterministic dynamical equations change into a series of nonlinear Langevin equations. Correspondingly, the main characteristics we explore will be investigated using non-equilibrium statistical concepts and methods, rather than chasing stochastic trajectories that stem from diverse initial conditions. The Langevin equation (LE) investigates the statistical characteristics of the system's trajectories. We can equivalently transform it to the probability distribution of the entire state space at a given time. It allows us to study the Fokker–Planck diffusion equations that can be deduced from LEs to explore such open systems [22, 35, 36], namely

$$\frac{\partial P(\boldsymbol{x},t)}{\partial t} = -\sum_i \frac{\partial[F_i(\boldsymbol{x})P(\boldsymbol{x},t)]}{\partial x_i}$$

$$+ \sum_i \sum_j \frac{\partial^2[D_{ij}(\boldsymbol{x})P(\boldsymbol{x},t)]}{\partial x_i \partial x_j}. \qquad (3)$$

Here, $D_{ij}(\boldsymbol{x}) = \mathcal{D}\,G_{ij}(\boldsymbol{x})$. The detailed derivation is provided in the Appendix. It is noteworthy that, due to the application of additive and

isotropic Gaussian white noise, for the sake of theoretical convenience, we consider the diffusion matrix $G(\boldsymbol{x})$ to be an identity matrix. By imposing appropriate natural boundary conditions and ensuring sufficient decay in the outer region, we can explore the asymptotic behavior of the Fokker–Planck equation and derive the corresponding steady-state probability distribution. We use $P_{ss}$ to represent the aforementioned steady-state probability distribution (small "$ss$" denotes statistical steady states). Now, we define a probabilistic flux $\boldsymbol{J}$ that satisfies $\boldsymbol{J} = \boldsymbol{F}P - \nabla \cdot (\mathcal{D}GP)$. Combining this with (3), we obtain the probability conservation form of the Fokker–Planck equation $\frac{\partial P(\boldsymbol{x},t)}{\partial t} + \nabla \cdot \boldsymbol{J}(\boldsymbol{x},t) = 0$. When the system reaches a steady state after a sufficiently long time under appropriate boundary conditions, the probability density no longer changes with time. Then, we can easily infer that the divergence of the probabilistic flux vanishes, i.e., $\nabla \cdot \boldsymbol{J}_{ss} = 0$. Since we apply additive Gaussian white noise to the system to explore its global stability, the diffusion matrix $D$ is a constant matrix, indicating that the divergence of $D$ is zero ($\nabla \cdot D(\boldsymbol{x}) = 0$). We can then deduce the driving force of the system accordingly as

$$\boldsymbol{F} = \frac{\boldsymbol{J_{ss}} + \mathcal{D}(\nabla P_{ss})}{P_{ss}} = \frac{\boldsymbol{J_{ss}}}{P_{ss}} - \mathcal{D}\,\nabla U, \qquad (4)$$

where $\nabla U$ represents the gradient of the potential function $U$ associated with the system. By analogy to the Boltzmann law in equilibrium systems, we define the population probability potential $U$ as

$$U = -\ln\left(P_{ss}\right). \qquad (5)$$

The newly defined non-equilibrium potential $U$ reflecting the weight of the states offers a clear physical interpretation and enables the evaluation of global stability and behavioral characteristics. The landscape, which corresponds to the three-dimensional (3D) topographical structure of $U$, plays a crucial role in landscape and flux theory. The presence of basins and barriers within this landscape allows for a comprehensive depiction of global stability and the probability distribution of all states. Based on the deductions mentioned earlier, we successfully decompose the system's driving force into two components. According to (4), the first component is associated with the steady-state probabilistic flux $\boldsymbol{J}_{ss}$ and the density of the probability distribution $P_{ss}$, while the second component is related to the gradient of the potential landscape $U$. In a steady state, the probabilistic flux has zero divergences, indicating two representing scenarios: (i) when the net input or output is zero, the system maintains detailed balance, and (ii) when the flux is non-zero, but with zero divergences, the system experiences a non-equilibrium state with broken detailed balance. Non-zero, divergence-free flux is a hallmark of non-equilibrium systems [20]. It can be viewed as a rotational and curl flux. The dynamics of non-equilibrium systems are co-determined by both the non-equilibrium potential and the curl flux, resembling the motion of electrons in an electric field (characterized by the potential gradient) and a magnetic field (reflected by the curl flux).

## 2.3. Non-equilibrium thermodynamics, average probability flux, and dissipative-dependent EPR

For non-equilibrium systems, an intriguing question is the specific degree of departure from equilibrium. This can be characterized using several specific quantities. As discussed earlier, non-zero yet divergence-free rotational flux serves as a distinctive signature of non-equilibrium systems, and substantial evidence suggests its intimate correlation with the existence of non-equilibrium energy pumps. This flux plays a pivotal role in maintaining the stability of the limit cycle oscillations within non-equilibrium systems [19–26, 37]. Inspired by this, we can define an average probabilistic flux $J_{av} = \frac{\int \mathrm{d}\boldsymbol{x}\,|\boldsymbol{J}_{ss}|}{\int \mathrm{d}\boldsymbol{x}}$ to quantify the global non-equilibrium extent of a system. Moreover, in non-equilibrium systems, energy consumption and dissipation are inevitable. The energy dissipation, which is associated with the entropy production rate in the steady state of the non-equilibrium system, serves as a global physical characteristic for measuring the system's departure from equilibrium. For non-equilibrium systems, the change in entropy over time can be divided into two parts, i.e.,

$$\frac{\mathrm{d}S}{\mathrm{d}t} = -\frac{\mathrm{d}}{\mathrm{d}t} \int \mathrm{d}\boldsymbol{x}\; P(\boldsymbol{x},t) \ln\left(P(\boldsymbol{x},t)\right) =$$

$$\int \frac{\mathrm{d}\boldsymbol{x}\,(\boldsymbol{J}\cdot(\mathcal{D}G)^{-1}\cdot\boldsymbol{J})}{P} - \int \mathrm{d}\boldsymbol{x}\,(\boldsymbol{J}\cdot(\mathcal{D}G)^{-1}\cdot\boldsymbol{F}_{eff}) =$$

$$S'_t - S'_e, \qquad (6)$$

where the entropy production rate (EPR) $S'_t = \int \mathrm{d}\boldsymbol{x}\;\frac{(\boldsymbol{J}\cdot(\mathcal{D}G)^{-1}\cdot\boldsymbol{J})}{P}$ is non-negative. It represents the total entropy change in the system and its surroundings and always obeys the second law of thermodynamics. On the other hand, the heat dissipation rate or the entropy flow rate $S'_e = \int \mathrm{d}\boldsymbol{x}\,(\boldsymbol{J}\cdot(\mathcal{D}G)^{-1}\cdot(\boldsymbol{F} - \mathcal{D}\nabla\cdot G))$ can be positive or negative, taking into account the energy and information flow between the system and its environment, leading to an increase or decrease in the system's entropy, respectively. Hence, the entropy of a non-equilibrium system does not necessarily always increase or maximize, while the total entropy production is always positive. We define the effective force $\boldsymbol{F}_{eff}$ as $\boldsymbol{F}_{eff} = \boldsymbol{F} - \mathcal{D}\nabla\cdot G$ [20–22, 25, 38].

## 2.4. Time irreversibility of the cross-correlation function and critical slowing down

The average difference between the forward-in-time and backward-in-time cross-correlation of two random sequences enables us to evaluate the extent

of detailed balance breaking and quantify the time irreversibility of a non-equilibrium system [26, 37]. It can be calculated as

$$\Delta CC = \sqrt{\frac{1}{t_f} \int_0^{t_f} \mathrm{d}\tau \left( C_{XY}(\tau) - C_{YX}(\tau) \right)^2}, \quad (7)$$

where $C_{XY}(\tau)$ and $C_{YX}(\tau)$ present the forward-in-time cross-correlation function and backward-in-time cross-correlation function, respectively. Here, $C_{XY}(\tau) = \langle X(0)Y(\tau) \rangle = \sum X^i Y^j P_i^{ss} P_{ij}(\tau)$ ($i, j$ are used to denote different states); $P_i^{ss}$ is the value of steady-state probability at state $i$; $P_{ij}(\tau)$ represents the probability of the system transitioning from state $i$ to state $j$ within a time interval $\tau$. Additionally, $C_{XY}(\tau) - C_{YX}(\tau) = X^A Y^B (P_A^{ss} P_{AB}(\tau) - P_B^{ss} P_{BA}(\tau)) = X^A Y^B J_{AB}^{ss} \tau$, (when $\tau$ is small) [24, 26, 35]. Evidently, the disparity between the forward-in-time and backward-in-time cross-correlation functions is intricately linked to the level of the steady-state probabilistic flux or the degree of detailed balance breaking.

Neurons can demonstrate abrupt transitions or systemic shifts, such as the shift from a resting state to the firing of an action potential. This occurrence is commonly referred to as a critical transition. As the system approaches a critical transition point, the internal dynamics would undergo a state transition. During this phase, alterations in the auto-correlation function often reveal notable features, such as increased and prolonged temporal correlations. This insight encourages the use of the auto-correlation function analysis, offering clues into the internal dynamics as the system approaches a critical state. This approach serves as a quantitative measure of the critical slowing down behavior.

## 3. Results and discussion

### 3.1. Linear stability analysis of the Hodgkin–Huxley model

To investigate the different states of a single neuron, we start with linear stability analysis and use MATLAB to find numerical solutions. This analysis helps us predict the long-term behavior and stability of the system under different parameter conditions. Explanations and default values of constants in the HH equations, unless otherwise specified, are provided in Table I [5, 39].

Linear stability analysis is a method used to study the stability of deterministic dynamic systems described by differential or difference equations. Numerous researchers have extensively explored the linear stability analysis of the HH model [7, 40]. Here, we summarize the key findings of the linear stability analysis of the HH model.

The basic steps involve finding equilibrium points, linearizing dynamic equations, calculating the Jacobian matrix, and determining eigenvalues

to assess stability. The Jacobi matrix is a matrix of partial derivatives that describes the linearized dynamics of the model around an equilibrium point. During linear stability analysis, the stability of the equilibrium points is determined by examining the real and imaginary eigenvalue parts of that the Jacobi matrix. If all eigenvalues have negative real parts, the equilibrium point is stable. If one or more eigenvalues have positive real parts, the equilibrium point is unstable. If there are eigenvalues with zero real parts and non-zero imaginary parts, further analysis may be required. Such equilibrium points are considered non-hyperbolic, and the geometric structure near these points may change. This behavior is known as a bifurcation at non-hyperbolic point. The Jacobian matrix of the HH model (see (10) and (11) in Appendix) can be represented as

$$\mathcal{J}_{\mathrm{Jacobi}} = \begin{bmatrix} \frac{\partial f_1}{\partial V} & \frac{\partial f_1}{\partial m} & \frac{\partial f_1}{\partial h} & \frac{\partial f_1}{\partial n} \\ \lambda_m m'_\infty & -\lambda_m & 0 & 0 \\ \lambda_h h'_\infty & 0 & -\lambda_h & 0 \\ \lambda_n n'_\infty & 0 & 0 & -\lambda_n \end{bmatrix}, \quad (8)$$

where $\lambda_x = \alpha_x(V) + \beta_x(V)$ and $x_\infty = \frac{\alpha_x(V)}{\alpha_x(V) + \beta_x(V)}$. Here, $x$ can be replaced with $m$, $h$, $n$. The detailed derivation can be found in the Appendix. In Table II, we present the eigenvalues denoted as $\lambda_i$ for $i = 1, 2, 3, 4$. To investigate the stability of the system, we apply the linear stability analysis method. This analysis identifies critical points where the stability of the system exhibits a qualitative change, known as a bifurcation. We can determine the system's stability under different conditions by examining the signs of the corresponding eigenvalues $\lambda$. It is observed that when $I < 9.7796 \ \mu\mathrm{A/cm}^2$ and $I > 154.5266 \ \mu\mathrm{A/cm}^2$, the states of the system are stable. In other words, the system will remain in its steady state under these specific current conditions.

To gain a comprehensive understanding of the dynamic behavior and stability of the HH model, and to visually illustrate the formation and evolution of attractors, we employed the MatCont software to generate a bifurcation diagram with the parameter $I$ as the bifurcation parameter.

Figure 1a presents a bifurcation diagram with $I$ as the bifurcation parameter, ranging from $I = -18 \ \mu\mathrm{A/cm}^2$ to $I = 200 \ \mu\mathrm{A/cm}^2$. Solid gray lines represent stable steady states, corresponding to stable resting states of neurons in physiology, denoted as SRS, while dashed gray lines represent unstable steady states, denoted as URS. As $I$ increases, a subcritical Hopf bifurcation, denoted as H1, occurs. Stable limit cycle oscillations are shown by the maximum (solid orange line) and minimum (solid yellow line) $V$ values, labeled as SLC. Unstable limit cycle oscillations are also shown by the maximum (scattered orange dots) and minimum (scattered yellow dots) $V$ values, labeled as ULC. The second Hopf bifurcation point is marked as H2. This visualization effectively elucidates the system's dynamic

TABLE I

Explanations and default values of parameters.

| Parameters | Explanation | Default values |
|---|---|---|
| $C_m$ | neuronal membrane capacitance | $1.0 \ \mu\text{F/cm}^2$ |
| $g_{Na}$ | sodium conductance | $120 \ \text{mS/cm}^2$ |
| $g_K$ | potassium conductance | $36 \ \text{mS/cm}^2$ |
| $g_L$ | leak conductance | $0.3 \ \text{mS/cm}^2$ |
| $V_{Na}$ | equilibrium potential of sodium ions | $115 \ \text{mV}$ |
| $V_K$ | equilibrium potential of potassium ions | $-12 \ \text{mV}$ |
| $V_L$ | reversal potential for the leak current | $10.599 \ \text{mV}$ |
| $\overline{\alpha_m}$ | constant related to the transfer rate of activating molecules (closed → open), denoted as $\alpha_m$ | $0.1 \ \text{ms}^{-1}$ |
| $\overline{\beta_m}$ | constant related to the transfer rate of activating molecules (open → closed), denoted as $\beta_m$ | $4.0 \ \text{ms}^{-1}$ |
| $vm$ | equilibrium potential of activating molecules | $25.0 \ \text{mV}$ |
| $K_{\alpha m}$ | dimensionless constant related to $\alpha_m$ | $10.0$ |
| $K_{\beta m}$ | dimensionless constant related to $\beta_m$ | $8.0$ |
| $\overline{\alpha_h}$ | constant related to the transfer rate of inactivating molecules (open → closed), denoted as $\alpha_h$ | $0.07 \ \text{ms}^{-1}$ |
| $\overline{\beta_h}$ | constant related to the transfer rate of inactivating molecules (closed → open), denoted as $\beta_h$ | $1.0 \text{ms}^{-1}$ |
| $vh$ | equilibrium potential of inactivating molecules | $30.0 \ \text{mV}$ |
| $K_{\alpha h}$ | dimensionless constant related to $\alpha_h$ | $20.0$ |
| $K_{\beta h}$ | dimensionless constant related to $\beta_h$ | $10.0$ |
| $\overline{\alpha_n}$ | constant related to the transfer rate of each subunit gate (closed → open), denoted as $\alpha_n$ | $0.01 \ \text{ms}^{-1}$ |
| $\overline{\beta_n}$ | constant related to the transfer rate of each subunit gate (open → closed), denoted as $\beta_n$ | $0.125 \ \text{ms}^{-1}$ |
| $vn$ | equilibrium potential of each subunit gate | $10.0 \ \text{mV}$ |
| $K_{\alpha n}$ | dimensionless constant related to $\alpha_n$ | $10.0$ |
| $K_{\beta n}$ | dimensionless constant related to $\beta_n$ | $80.0$ |

TABLE II

Numerical results for stability analysis.

| $I$ | $V_0$ | $m_0$ | $h_0$ | $n_0$ | $\lambda_1$ | $\lambda_2$ | $\lambda_3$ | $\lambda_4$ |
|---|---|---|---|---|---|---|---|---|
| 0.0000 | 0.0000 | 0.0529 | 0.5961 | 0.3177 | $-4.6753$ | $-0.20 + 0.38\text{i}$ | $-0.20 - 0.38\text{i}$ | $-0.1207$ |
| 5.0000 | 3.2667 | 0.0772 | 0.4794 | 0.3687 | $-4.5975$ | $-0.10 + 0.52\text{i}$ | $-0.10 - 0.52\text{i}$ | $-0.1292$ |
| 9.7796 | 5.3459 | 0.0973 | 0.4062 | 0.4018 | $-4.7643$ | $0.5862\text{i}$ | $-0.5862\text{i}$ | $-0.1385$ |
| 120.0000 | 19.8776 | 0.3661 | 0.0886 | 0.6175 | $-8.7149$ | $0.15 + 0.97\text{i}$ | $0.15 - 0.97\text{i}$ | $-0.2810$ |
| 154.0000 | 21.9132 | 0.4189 | 0.0706 | 0.6429 | $-9.4024$ | $0.0024 + 1.0618\text{i}$ | $0.0024 - 1.0618\text{i}$ | $-0.3104$ |
| 154.5266 | 21.9419 | 0.4197 | 0.0704 | 0.6432 | $-9.4121$ | $1.0629\text{i}$ | $-1.0629\text{i}$ | $-0.3109$ |
| 155.0000 | 21.9677 | 0.4204 | 0.0702 | 0.6436 | $-9.4208$ | $0.0021 + 1.0640\text{i}$ | $0.0021 - 1.0640\text{i}$ | $-0.3113$ |
| 180.0000 | 23.2537 | 0.4544 | 0.0609 | 0.6588 | $-9.8554$ | $-0.11 + 1.11\text{i}$ | $-0.11 - 1.11\text{i}$ | $-0.3310$ |

behavior as the parameter $I$ varies, including the presence of stable and unstable periodic solutions and their relationship to stable and unstable steady states.

At the top corner of panel (a), the nested inset plot depicts the phase states of the system for different bifurcation parameter ranges. The dark blue vertical line marks the boundary between stable steady states and stable limit cycles, labeled $I_0$. The purple vertical line represents the $I$ value of H1, denoted as I1, while the red vertical line, marked as I2, indicates the boundary between stable limit cycles and stable resting states at H2. Through calculation, we obtain $I_0 = 6.2645 \ \mu\text{A/cm}^2$, $I_1 = 9.7796 \ \mu\text{A/cm}^2$, and $I_2 = 154.5266 \ \mu\text{A/cm}^2$. These three vertical dividing lines delineate distinct states within the system. In Fig. 1a, B represents the bistable region of the classical HH model,
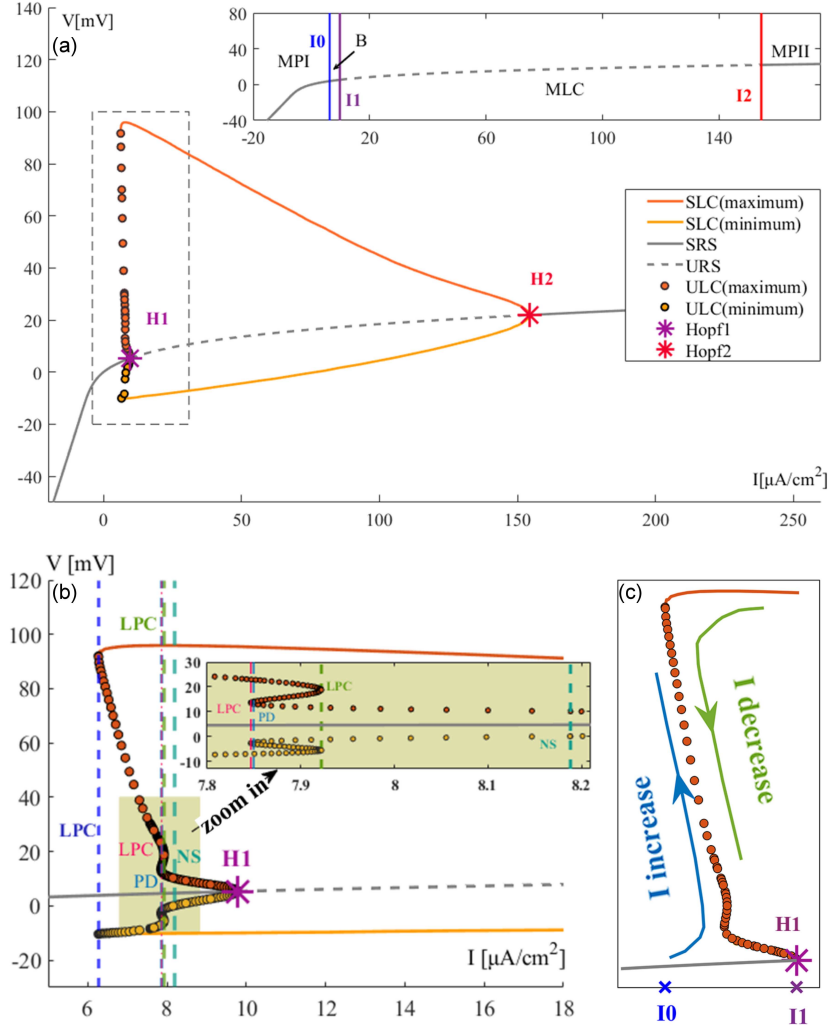
Fig. 1. Deterministic bifurcation diagram. (a) Overall bifurcation diagram with $I$ as the bifurcation parameter. The solid orange line shows the maximum $V$ value within the stable limit cycle (SLC), while the solid yellow line shows the minimum $V$ value within SLC. The solid gray line represents a stable resting state, denoted as SRS. The dashed gray line represents an unstable resting state, denoted as URS. The scattered orange dots denote the maximum value of $V$ within the unstable limit cycle (ULC), while the scattered yellow points represent the minimum value of $V$ within ULC. Here, H1 is the first Hopf bifurcation point and H2 is the second Hopf bifurcation point. The axes embedded above are a simplified diagram of the overall bifurcation plot. The dark blue vertical line is marked as $I_0$, the purple vertical line is marked as $I_1$, and the red vertical line is marked as $I_2$. MPI signifies the region $I < I_0$, where neurons are in a stable resting state, while MPII represents the stable resting state when $I > I_2$. The region between $I_0$ and $I_1$ is denoted as B, indicating the bistable region where neurons oscillate between SRS and SLC. MLC denotes the parameters region that the system undergoes a mono-stable limit cycle, which is between $I_1$ and $I_2$. (b) Local dynamical bifurcation detail illustration of the bistable region in the HH model. The dark blue vertical dashed line indicates the limit point bifurcation of cycles (LPC) at the boundary, where one stable limit cycle and one unstable limit cycle merge into a single limit cycle. The coordinate area inserted in the upper right corner is an enlarged illustration of the yellow rectangular area to the right of the dark blue LPC. It includes a pink vertical dashed line indicating LPC at the boundary, where two unstable limit cycles merge into one unstable limit cycle, while the blue vertical dashed line represents the period-doubling bifurcation, labeled PD. The green vertical dashed line marks another occurrence of LPC. The fluorescent green vertical dashed line represents the Neimark–Sacker (NS) bifurcation. (c) Dynamical evolution diagram of the HH neuron near H1 without noise. The blue solid line with arrows indicates the evolution direction of the dynamic state near H1 as $I$ gradually increases, while the green solid line with arrows represents the dynamic evolution path as $I$ gradually decreases. The solid gray line represents a stable resting state. The scattered orange dots show the maximum value of $V$ during oscillations of ULC, providing a simplified representation of different ULC. The solid orange line represents the maximum value of $V$ during stable limit cycle oscillations, providing a simplified representation of different SLC. The relative positions of $I_0$ and $I_1$ are marked with dark blue and purple crosses, respectively.

and MLC signifies a singular stable limit cycle region. Additionally, we denote the region $I < I_0$ as MPI and the region $I > I_2$ as MPII, corresponding to regions of stable resting states.

Figure 1b provides an enlarged view of the dashed rectangular region in panel (a), including a further magnified illustration that illustrates multiple bifurcations from stable resting states to stable limit cycles. Discrete orange and yellow dots represent, respectively, the maxima and minima of the unstable limit cycles, while vertical dashed lines mark the locations of bifurcations. The limit point bifurcation is a critical phenomenon in nonlinear dynamical systems. It involves the transition of equilibrium or periodic solutions (limit cycles) from stable to unstable states, or vice versa. This process can give rise to new stable solutions or the disappearance of existing ones. The term "limit point bifurcation of cycles" (LPC) specifically denotes this behavior in the context of periodic solutions (limit cycles). The emergence of LPC indicates a change in the characteristics or numbers of limit cycles. In panel (b), LPC at $I = I_0 = 6.2645 \ \mu\text{A}/\text{cm}^2$ (dark blue vertical dashed line) indicates the merging of the stable limit cycle and the unstable limit cycle into a single limit cycle. LPC at $I = 7.9220 \ \mu\text{A}/\text{cm}^2$ (green vertical dashed line) represents the merging of a unstable limit cycle with a relatively large amplitude with another an unstable limit cycle with relatively small amplitude into an unstable limit cycle with an amplitude between the two. LPC at $I = 7.8465 \ \mu\text{A}/\text{cm}^2$ (pink vertical dashed line) is similar to LPC at green vertical dashed line, indicating the merging of two unstable limit cycles into one unstable limit cycle. For simplification, we will refer to LPCs occurring at different currents by their colors. For example, LPC corresponding to a dark blue vertical dashed line is simplified as a dark blue LPC. PD denotes the period doubling (flip) bifurcation, happening at $I = 7.8495 \ \mu\text{A}/\text{cm}^2$ (blue vertical dashed line). When switching from the PD point to another branch, the period of the unstable limit cycle undergoes a sudden doubling. And NS, i.e., the Neimark–Sacker (secondary Hopf) bifurcation, occurs at $I = 8.1882 \ \mu\text{A}/\text{cm}^2$ (mint green vertical dashed line) [41, 42]. In the upper right corner of panel (b), the inserted subplot provides an enlarged illustration of the yellow rectangular area to the right of the dark blue LPC. This is to get a clearer representation of the detailed dynamics within the interval $7.8 < I < 8.21 \ \mu\text{A}/\text{cm}^2$ and to offer a clearer distinction of bifurcation positions in this range.

Dynamical evolution trends near H1 are depicted in panel (c). The solid gray line represents the stable resting state. The scattered orange dots represent the maximum values of $V$ during the oscillations of the unstable limit cycles, providing a simplified representation of the different unstable limit cycles. The solid orange line represents the maximum values of $V$ during stable limit cycle

oscillations, simplifying the representation of different stable limit cycles. As the bifurcation parameter $I$ gradually increases from a value below $I_0 = 6.2645 \ \mu\text{A}/\text{cm}^2$ and goes across $I_1 = 9.7796 \ \mu\text{A}/\text{cm}^2$ (corresponding to the first Hopf bifurcation point H1), the system evolves overall along the direction of the blue arrow, switches from the stable resting state represented by the solid gray line to H1, and then to the unstable limit cycle indicated by the scattered orange dots, and ultimately reaches the stable limit cycle represented by the solid orange line. In this process, the Hodgkin–Huxley neuron undergoes a sequence of bifurcations: from a stable resting state to H1, further to NS (where $I = 8.1882 \ \mu\text{A}/\text{cm}^2$), then to the pink LPC, followed by PD (where $I = 7.8495 \ \mu\text{A}/\text{cm}^2$), and then to the green LPC, further reaching the dark blue LPC, and eventually entering the stable limit cycle oscillations. The HH neuron will evolve in the direction of the green arrow in Fig. 1c, sequentially undergoing processes starting from the stable limit cycle represented by the solid orange line, to the unstable limit cycle represented by the scattered orange dots, and eventually reaching the stable resting state represented by the solid gray line. During this whole process, a series of bifurcations will take place (see Fig. 1b): the system first reaches the dark blue LPC, through PD to the green LPC, then to the pink LPC, further to NS, and it eventually reaches a stable resting state. This explains why, without noise, the system only reaches limit cycles after passing H1 by gradually increasing the current $I$. When $I_0 < I < I_1$ is fulfilled, a coexistence of SRS and SLC emerges, involving: a large amplitude stable limit cycle, one to three small-amplitude unstable limit cycles, and a stable resting state. Particularly, in the region between pink LPC and the green LPC, where multiple unstable limit cycles appear, we designate it as the $w$ interval. The complex dynamics within this interval are key features that distinguish the classic HH model from a series of simplified HH models, such as the Morris–Lecar (ML) model [7]. Eventually, the unstable limit cycle disappears at $I_1$. At the endpoint zone MPII, a single steady-state solution exists. This result demonstrates that when the stimulus current is too high, the cell becomes inactive or dies, illustrating the importance of parameter regulation for cellular dynamics. The discussions presented above are conducted under the conditions of deterministic equations.

### 3.2. Landscape and flux of a Hodgkin–Huxley neuron

We now explore the application of the landscape–flux approach to neuronal dynamics by investigating the HH model with Gaussian white noise (see (1)). When we apply Gaussian white noise
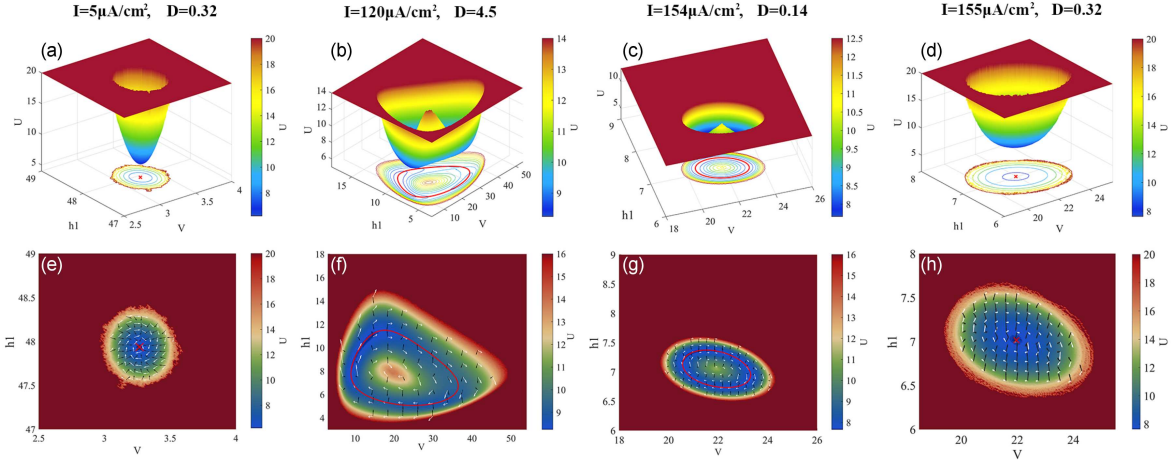
Fig. 2. The underlying potential landscapes and patterns of curl flux distribution evolve as the bifurcation parameter $I$ increases under varying intensities of Gaussian white noise. Values of stimulus current $I$ and noise intensity $\mathcal{D}$ are shown at the top of each panel. Panels (a)–(d) show 3D landscapes under different stimulus currents and fluctuation strengths. Panels (e)–(h) show 2D dimensional contour plots of the landscapes and steady-state fluxes under different stimulus currents and fluctuation strengths. In panels (a) and (d), the red "cross" indicates the single stable attractor corresponding to the deterministic equations. In panels (b) and (c), the red circles represent the stable limit cycles of the deterministic equations under the condition of a given stimulus current and noise intensity. Panels (e)–(h) illustrate the distribution of non-equilibrium driving forces under the conditions corresponding to the top ones. The white arrows represent the steady-state probabilistic curl flux, while the black arrows depict the landscape gradient distribution.

simultaneously in each dimension, then we use a one-dimensional array $\boldsymbol{A_\Gamma} = [A_V, A_m, A_h, A_n]$ to scale the magnification of the same noise intensity in different dimensions. We establish the corresponding probabilistic diffusion equation to obtain statistically steady-state probability distributions in the state space of the system. As the HH model is inherently four-dimensional, directly visualizing its potential landscape poses challenges. Thus, we focus on two key variables in the model, namely $V$ and $h1$, while integrating the remaining variables to depict the comprehensive features of a single neuron on a global scale.

Figure 2 shows the three-dimensional and two-dimensional (2D) potential landscape, as well as the driving forces' distribution of the HH neuron for different values of the bifurcation parameter $I$, with the dimension noise amplification matrix set to $\boldsymbol{A_\Gamma} = [1.0, 0.0001, 1.0, 0.0001]$. Notably, for computational convenience, we have introduced the variable $h1 = 100h$ to facilitate the depiction of the corresponding potential landscape. When $I = 5\,\mu\text{A/cm}^2$ and $\mathcal{D} = 0.32$, we evenly distributed $20 \times 23$ initial points across the $(V, h1)$ plane and tracked their trajectories from $t = 0$ to $t = 108\,315\,000$. Subsequently, we collected sample points from all trajectories between $t = 2\,500\,000$ and $t = 108\,315\,000$ to compute the probability distribution $P$. Then, we further calculated the probability distribution $P$ for all trajectories between $t = 3\,000\,000$ and $t = 108\,315\,000$ and compared the results of these two computations. We found that $P$ was the same for both calculations. Therefore, we hypothesize

that the system reaches a non-equilibrium steady state after $t = 3\,000\,000$ time steps. Unless stated otherwise, we collected sample points for analysis by tracking trajectories from $20 \times 23$ initial points on the $(V, h1)$ plane, starting from $t = 3\,000\,000$ onwards. As depicted in Fig. 2a, when Gaussian white noise is introduced and in the context of a long-time limit, the uniqueness of the steady-state solutions in the deterministic equation diminishes. Instead, the final distribution of the global states assumes a funnel-shaped configuration. The stable resting state solution of the deterministic equation (marked by a red cross in the figure) resides at a local minimum of $U$, which indicates the maximum probability within the overall state distribution. In panel (e), the corresponding driving forces of the system under the conditions outlined in panel (a) are elucidated. The black arrows signify the force arising from the negative gradient of the potential landscape, consistently propelling the system's instantaneous state towards states of higher probability. Globally, the gradient force continually attracts the system toward the lowest point of the potential landscape funnel. The white arrows symbolize the probabilistic curl flux, which can be observed rotating around the single stable attractor, attempting to perturb the instantaneous state in conjunction with the gradient force. This effectively disrupts the point attractor and holds the capacity to trigger the emergence of new states. Besides, through the combined action of probabilistic curl flux, the system is not solely dragged by the gradient force directly to the bottom of the funnel. Instead, it

spirals down towards the attractor basin. This illustrates the essential interplay between both factors in maintaining the dynamics of non-equilibrium systems.

In Fig. 2b and c, the potential landscapes associated with a singularly stable limit cycle oscillation are illustrated. The topography of these landscapes resembles a Mexican hat, with the steady-state curl flux in the ring valley prominently overshadowing the influences exerted by the steady-state non-equilibrium potential's negative gradient. This dominance of probabilistic flux plays a vital role in sustaining the stability of the periodic oscillatory behavior. In two panels (b) and (c), the red circles represent the limit cycles of stable periodic oscillations under each respective input current ($I = 120~\mu\mathrm{A/cm^2}$ in (b), and $I = 154~\mu\mathrm{A/cm^2}$ in (c)) in the absence of noise. Panels (f) and (g) depict the distributions of driving forces in non-equilibrium systems, corresponding to those illustrated in (b) and (c). In panels (f) and (g), the white arrows denote the curl flux components of the non-equilibrium driving forces, whereas black arrows represent the negative gradient part of these driving forces. The red circles in these panels also denote the limit cycles for stable periodic oscillations, specific to each input current in the noise-free setting. Notably, in the vicinity of these limit cycles, the probabilistic curl flux is observed to align parallelly. This observation provides a detailed explanation of the previously mentioned phenomenon, namely the stability of the periodic oscillations is maintained due to the steady-state curl flux within the ring valley significantly surpassing the influence of the steady-state non-equilibrium potential's negative gradient.

As the bifurcation parameter $I$ increases, neuronal behavior switches from periodic oscillations to a non-firing state, which biologically corresponds to neuronal inactivation or even cell death. Figure 2d depicts the potential landscape topography at the electrical current $I = 155~\mu\mathrm{A/cm^2}$, which is just after the second Hopf bifurcation point H2, where neurons are incapable of discharging. The topography is similar to that explained in panel (a), but with a noticeably larger and broader funnel structure at the same noise intensity of $\mathcal{D} = 0.32$. It is conceivable that in a range where the current value $I$ exceeds the second Hopf bifurcation point H2, the landscape funnel would become progressively sharper and narrower as the $I$ values increase, for the same noise intensity. Panel (h) describes the distribution of the system's driving forces corresponding to (d). In a low-noise environment, the probabilistic flux continues to be rotational; however, the role of the negative gradient of the steady-state non-equilibrium potential grows more pronounced compared to the circulatory effect. The system state would follow a downward spiral trajectory to the lowest point of the potential landscape funnel configuration, marked by the red cross in panels (d) and (h). This point corresponds to the resting state of the neuron at the input current $I = 155~\mu\mathrm{A/cm^2}$ in a noise-free scenario.

### 3.3. A quantitative assessment of the system's stability and robustness under a noisy background

Next, we investigate the impact of noise on neurons within the MPI parameter set (i.e., in the region $I < I_0$). The noise intensity coefficients are denoted by $\boldsymbol{A_\Gamma} = [100.0, 0.0001, 0.1, 0.0001]$. When $I = -10~\mu\mathrm{A/cm^2}$, as depicted in Fig. 1, the deterministic HH neuron is in the MPI parameter regime and will remain in the resting state without external stimulation. We collected simulated time series data of the membrane potential $V$ under noise intensities $\mathcal{D} = 0.45$ and $\mathcal{D} = 0.01$ at $I = -10~\mu\mathrm{A/cm^2}$. It was observed that noise with the intensity of $\mathcal{D} = 0.45$ could trigger action potentials in the HH neuron, while noise with an intensity of $\mathcal{D} = 0.01$ could not facilitate the generation of action potential. This indicates that sufficiently high noise intensity can help the HH neuron to depart from the resting state and fire an action potential earlier compared to the deterministic HH neuron. Subsequently, we will focus on exploring the underlying dynamics of the HH neuron at noise intensities that can facilitate action potential firing in the MPI parameter set. As an example in our investigation, we will use the noise intensity $\mathcal{D} = 0.45$ at $I = -10~\mu\mathrm{A/cm^2}$. Figure 3a illustrates the transition of HH neurons under the MPI parameters from a resting state to spike generation in the presence of sufficiently intense finite noise. Starting from the resting state corresponding to $I = -10~\mu\mathrm{A/cm^2}$, the dynamic process lasts sufficiently long. After reaching a statistically steady state, we gather all trajectories and states that occurred in the dynamic process in the sufficient time. The collection of all trajectories and states is plotted as a final two-dimensional mapping of the potential landscape. The white dashed line signifies a threshold division, where the points on the left are directly pulled back to the resting state by the system's driving force, while the points on the right complete a cycle under the driving force, indicating the generation of action potential. This illustrates the neuron's sensitivity to a threshold. This corresponds to a phenomenon commonly observed in fast-spiking cells when subjected to appropriate current stimulation, characterized by intermittent switching between low-frequency periodic firing and a resting state [43]. When noise leads the HH neurons to go beyond the threshold, the phase trajectory can follow a circular path back to the resting state under the influence of curl flux. Subsequently, the system further assesses the possibility of crossing the threshold again based on the real-time noise contributions. Another action

potential occurs when the neuron's parameters successfully go cross the threshold again. However, if the noise fails to assist the neuron in crossing the threshold, it can directly return to the resting state rather than completing a circular path. As a result, competitive dynamic emerges between the resting state and the circular limit cycle under sustained noise influence. The unpredictability of noise presents a challenge in maintaining continuous, sustained discharges, ultimately resulting in an overall low-frequency firing pattern. Hence, a competitive dynamic emerges between the resting state and the circular limit cycle under sustained noise influence.

Figure 3b illustrates the probabilistic flux distribution of the system once it reaches a statistically steady state, where the distribution aligns nearly parallel to the direction of the system's driving force $\boldsymbol{F}$. In the low noise limit, the potential function linked to the gradient part of the driving force resembles a Lyapunov function in deterministic dynamics. The points where the gradient of this potential function hits zero act as attractors in deterministic dynamics. Here, the resting state and action potential correspond to stable points and limit cycles, respectively. The gradient force guides the system's trajectories toward the bottom region of the potential function, i.e., stable points and limit cycles. The driving force linked to the probabilistic flux facilitates transitions between different states in the system. Additionally, due to sufficiently small noise, the numerical value of the gradient force is typically orders of magnitude smaller than the driving force associated with the probabilistic flux. This results in a distribution of the probabilistic flux closely resembles the overall driving force distribution of the system. The oscillation period can be approximated by the loop integral of $\boldsymbol{J}_{ss}/P_{ss}$ along the circular oscillation path [19].

It can be seen from (5) that the smaller the value of $U$, the greater the probability of the corresponding state. The resting state precisely sits at the lowest point of the entire potential landscape, marked as $U_{\text{rest}}$. The population probability potential $U$ corresponding to the threshold can be represented using the minimum value of $U$ on the white dashed line, labeled $U_{\text{thresh}}$. When a neuron transitions from the resting state to firing an action potential, it needs to jump from the lowest level to the height of $U_{\text{thresh}}$ of the potential landscape. We use $\Delta U = U_{\text{thresh}} - U_{\text{rest}}$ to measure the barrier height between two states. Figure 4a illustrates the trend of the corresponding barrier height as the bifurcation parameter changes. When subjected to noise of the same intensity, the resulting green curve represents a fitting curve of the data points, which takes the form of $a \exp(-b\,x) + c$ (where $a$, $b$, and $c$ are constants greater than zero). This indicates that as the stimulation current increses, the barrier height between the resting state and the firing action potential exhibits exponential reduction, making the
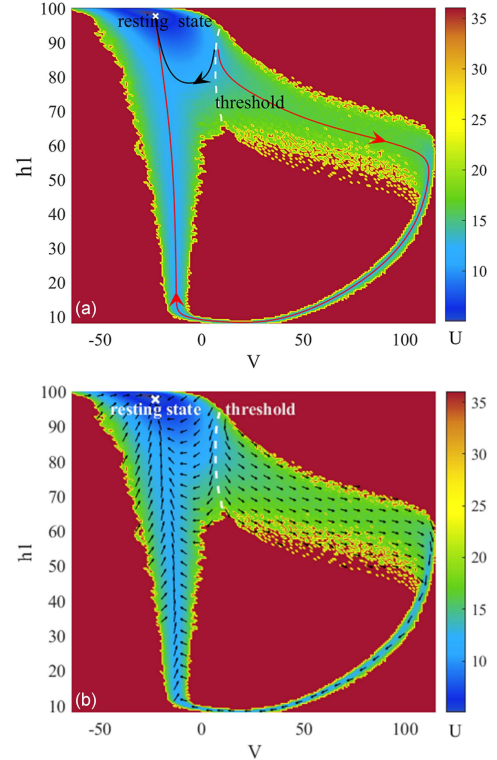


Fig. 3. The impact of noise on HH neuron dynamics. (a) HH neurons under MPI parameters compete between action potentials and subthreshold oscillations near the threshold. The white cross signifies the resting state. The black and red lines depict distinct driving force streamlines from two points near the threshold. The white dashed line separates the resting state from spikes, depicting the neuron's threshold ($I = -10 \ \mu\text{A/cm}^2$, $\mathcal{D} = 0.45$). (b) The distribution of probabilistic flux throughout the entire process. The direction of the black arrows represents the direction of the system's probabilistic flux.

transition from the resting state to the action potential easier. Therefore, the barrier height between the resting state and the action potential measures the difficulty of transitioning between these two states, serving as a quantification criterion to estimate the robustness of the resting state.

Under substantial Gaussian white noise, the HH neuron departs from its deterministic resting state, overcoming the height of the potential landscape, $\Delta U$, to reach the threshold potential for generating an action potential. This critical period, from the starting point until just beyond the threshold potential, moments before the action potential is initiated, represents the minimum duration needed for the HH neuron to escape its resting state, or represents the initial transition time from the resting state to the onset of an action potential. Concerning the potential landscape's topography, this duration signifies the time required to depart from the resting state's lowest point and reach
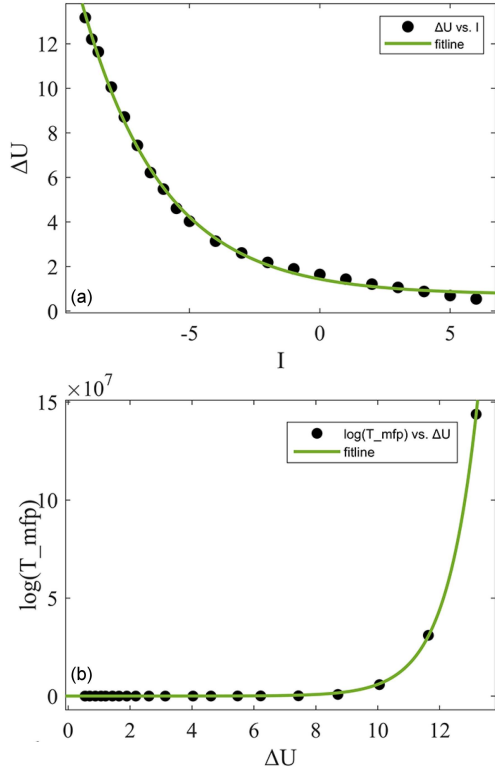
Fig. 4. Quantification of the transition difficulty of Hodgkin–Huxley neurons from the resting to the action potential state under MPI parameters. (a) Change in barrier height versus bifurcation parameter $I$ for the resting-to-action potential transition ($\mathcal{D} = 0.245$). (b) The logarithm of the mean first pass time needed to reach the action potential from the resting state as a function of barrier height ($\mathcal{D} = 0.245$).

$U_{\mathrm{thresh}}$ for the first time. We refer to this duration as the "first-passage time". By recording the first passage time repeatedly and calculating the average, we will get the mean first passage time (MFPT) — denoted as Tmfp. It offers another quantification of the stability of the system. Figure 4b illustrates the natural logarithm of Tmfp vs the barrier height $\Delta U$. Under the same noise intensity, the fitted curve exhibits an exponential trend (fitted formula $a\exp(bx)$, where both $a$ and $b$ are greater than 0). This indicates that as the barrier height increases, the required evolution time becomes longer, and the transition between different states becomes harder. Looking from left to right at the panel (b), the system becomes more and more stable. The quantitative fitting here shares a resemblance with the Arrhenius law observed in equilibrium systems.

For the MLC parameter set of the HH neuron, the comparative analysis between panels (b) and (c) in Fig. 2 reveals varying heights of the central island in the potential landscape, corresponding to different noise intensities and bifurcation parameters. To quantitatively determine the stability

of the system's limit cycle attractor, we relied on 3D potential landscapes to establish two barrier heights, which aided us in tracing the range of the limit cycle's path distribution in the state space. One barrier is the difference in population probability potential between the highest point on the central island in a Mexican hat and the lowest point along the circular path — it is denoted as Barrier1 $= U_0 - U_{\min}$; the other is the difference between the highest point of the central island and the value of $U$ at the maximum along the circular path, i.e., Barrier2 $= U_0 - U_{\max}$. For different bifurcation parameters under the same noise intensity, the height of the central island is correlated to the size of the corresponding red circle in the 2D phase space shown in panels (b), (c), (f) and (g) in Fig. 2. A larger circular area indicates the need for greater noise assistance or more statistical data points to reach the high points within the central island. Statistically, under the same noise intensity, it's easier to reach the central island with a smaller circular area, which naturally results in a smaller formed barrier height. Here, we study the stability of the system's limit cycle attractor under varying noise intensities applied to the same bifurcation parameter.

In Fig. 5a, the variations of two barrier heights, Barrier1 and Barrier2, vs the fluctuations of noise intensity are presented. The solid line corresponds to the difference in barrier heights along the upper boundary of the attractor of the limit cycle, labeled Barrier1. In contrast, the dashed line represents the Barrier signifying the lower boundary of the limit cycle. Both Barrier1 and Barrier2 decrease as the noise intensity scaling coefficient $\mathcal{D}$ increases. Panel (b) illustrates the relationship between the average first-passage time $\tau$ of the limit cycle attractor and barrier heights. The escape time increases with the barrier height. Thus, for the same input stimulus current, higher applied noise leads to smaller barrier heights and shorter average first-passage times from the limit cycle attractor, indicating greater instability of the limit cycle.

### 3.4. Entropy production, average probabilistic flux, and phase transitions

Considering the phase transition of the HH neuron with Gaussian white noise, we use the stimulus current $I$ as a changing parameter for comparison with a deterministic bifurcation diagram. Figure 6a displays the system's EPR and the average probabilistic flux $J_{av}$ variations with $I$ under finite-amplitude Gaussian white noise. Here, the scales of the two $y$ axes for flux (on the right) and EPR (on the left) are different. Before reaching the initial bifurcation point $I_1$, $J_{av}$ maintains relatively low values. It undergoes an abrupt increase at $I_1$, marking a discontinuous phase transition.
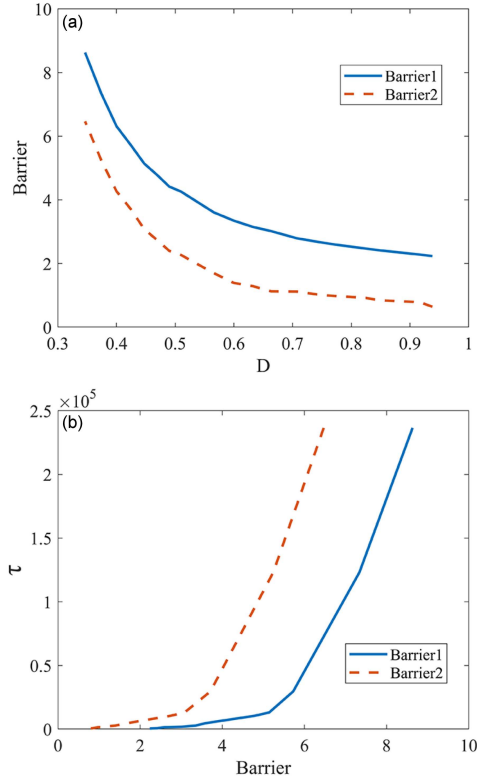
Fig. 5. Barrier heights and escape time in Hodgkin–Huxley neurons under MLC parameters. (a) Barrier heights $U_0 - U_{\min}$ and $U_0 - U_{\max}$ vs noise intensity for $I = 120\ \mu A/cm^2$. (b) Comparison of escape time with barrier heights for various noise intensities.

Subsequently, $J_{av}$ gradually decreases to zero at $I_2$, indicating a continuous phase transition within the system. However, as shown in Fig. 3, under sufficient finite noise conditions, the system experiences a transition period between the resting state and action potentials before $I_1$, corresponding to zone B in the deterministic bifurcation diagram. This suggests that due to noise influence, the system undergoes oscillations even before $I_1$. Why doesn't $J_{av}$ undergo a sudden change earlier?

We divided the entire state space into a grid of small $200 \times 200$ squares and tracked all trajectory points once the non-equilibrium steady state was reached. By calculating the average absolute values of the probabilistic flux $J_{\text{unit}}$ for each grid and summing these values throughout the system, we obtained the total absolute values of the probabilistic flux $J_{\text{total}}$. Dividing this by the total number of squares in the state space, we can get the average probabilistic flux $J_{av}$ over the entire state space. When the HH neuron is influenced by limited noise and is sufficiently distant from the Hopf bifurcation point H1 within the MPI parameter set, it will generate intermittent irregular action potentials (see Fig. 3). When the resting state coexists with periodic oscillations, reaching a non-equilibrium steady state, we partition the entire state space into two parts: the annular funnel region where the static points are situated, and the circular path formed by the limit cycle. To roughly estimate the average flux $J_{av}$ in this bistable state, we distinguish it into $J_{av-\text{funnel}}$ in the annular funnel region and $J_{av0}$ along the circular path. In the circular depression area where the resting state resides (we refer to Fig. 2e and h), $J_{av-\text{funnel}}$ exhibits no significant changes compared to $J_{av-I-\text{smaller}}$ observed when the periodic oscillations have not appeared. We isolated the circular path by excluding the funnel region around the resting state and computed the average probabilistic flux along this circular path using $J_{av0} = (\oint dl\ J)/(\oint dl)$. Subsequently, by dividing this value by the number of the spatial grid squares excluding the area around the resting state, we obtained $J_{av1}$ for the entire state space.

Interestingly, $J_{av0}$ exhibits a magnitude comparable to $J_{av}$ after the phase transition ($I$ is within the MLC range). The subsequent $J_{av1}$, on the contrary, is approximately four orders of magnitude smaller than $J_{av}$. Due to the limited noise and small stimulation current, the distribution of the resulting limit cycle in the state space is narrow. This limited spread prevents the formation of explicit central islands, as Fig. 2b and c, because trajectories corresponding to the intermediate region within the circular path cannot be reached. Although this is not a fundamental defect, the system, influenced by limited noise intensity and within a finite computational time (recorded at time $t = 108\,315\,000$), fails to reach states with a particularly small probability distribution near the vertices of the central islands. Consequently, this explains why the average probabilistic flux $J_{av1}$ across the entire state space does not undergo an immediate abrupt change when the resting state coexists with periodic oscillations in the system. EPR also experiences a sudden change at $I_1$ and then gradually approaches zero at $I_2$. This is due to the close relationship between the calculation of EPR and the probabilistic flux.

When looking at Fig. 2e–h and Fig. 3b, the gradient part of the system's driving force continuously directs the system state towards the bottom region of the potential landscape, stabilizing point attractors and limit cycles if they exist. Meanwhile, the curl flux, because of its rotational nature, tends to destabilize point attractors. Greater curl flux may render the original state less stable and can even alter the landscape's topography, finally generating new states, leading to a phase transition (as observed in Figs. 2e, 2f, and 3b). Together, these three mentioned panels of the figures capture the different stages of the entire process. Figure 2g and h vividly illustrates the less pronounced changes in the curl flux during a continuous phase transition. Hence, the curl flux plays a dynamic role in driving phase transitions or bifurcations/catastrophes in non-equilibrium systems.
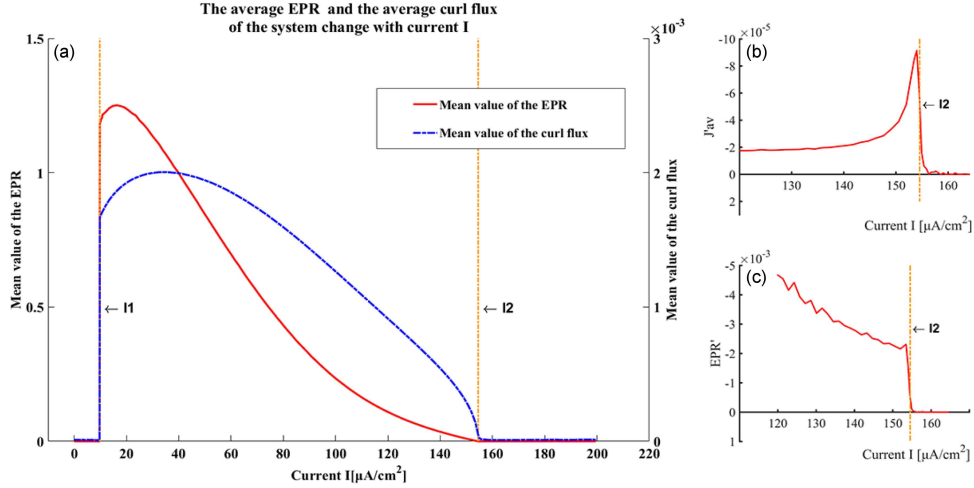
Fig. 6. EPR and the average probabilistic flux $J_{av}$. The solid red line represents the mean value of EPR across the entire state space. In contrast, the dashed blue line reflects the relationship between the system's average probabilistic flux $J_{av}$ and the bifurcation parameter. The noise intensity is set at $\mathcal{D} = 0.1$. The two vertical dashed lines correspond to the two Hopf bifurcation points, $I_1$ and $I_2$, in the deterministic bifurcation diagram. (b) First derivative of the average curl flux with respect to the stimulus current. (c) First derivative of EPR with respect to stimulus current.

The entropy production rate (EPR) quantifies irreversible processes within a system, indicating its tendency to move towards higher entropy states. When a non-equilibrium system reaches a statistically steady state after a sufficiently long time, the numerical value of EPR equals the system's heat dissipation rate or entropy flow rate $S_e'$. This equivalency allows EPR to describe the energy transfer within the system. Within the range of $I_0 < I < I_1$, as genuine limit cycles are not formed, neurons can only physiologically engage in low-frequency discharges, and therefore, EPR undergoes a sudden change only at $I = I_1$.

As for the second Hopf bifurcation point $I_2$, we calculated the first derivatives of the flux and EPR around $I_2$, as shown in Fig. 6b and c. We found that both the first derivatives of EPR and the flux show discontinuous changes at $I_2$, indicating a second-order phase transition at $I_2$. The physical meaning of the transition is that the neuron's steady states change from stable periodic oscillation to a stable resting state as the stimulus current increases. EPR can be considered as the thermodynamic origin of bifurcation or phase transition points in a non-equilibrium system. Both $J_{av}$ and EPR can serve as order parameters for bifurcations and phase transitions at $I_1$ and $I_2$ of the system.

### 3.5. Time irreversibility of the cross-correlation function and critical slowing down

For the practical side, the average flux and EPR are not always easy to quantify directly from experimental observations such as time se-

ries. However, the non-equilibrium nature can be extracted directly from the time asymmetry of the cross-correlations of the observables. If we consider a neuron operating under the influence of noise, receiving a constant stimulus current and reaching a statistically steady state as a non-equilibrium state, we can calculate the difference in two-point cross-correlation functions for the forward and reverse times. This method helps quantify the extent of detailed balance breaking and irreversibility of time within the system.

Figure 7a displays a time series plot of the neuron membrane potential $V$ and the parameter $h1$, representing the inactivation of sodium channels. With relatively small noise applied and operated at $I = 10$ $\mu A/cm^2$ within the MLC range, $V$ and $h1$ demonstrate overall stable periodic oscillations. However, setting the diffusion coefficient matrix $\boldsymbol{A_\Gamma}$ to $[100.0, 0.0001, 0.1, 0.0001]$ results in maximal noise intensity imposed on $V$, leading to more pronounced jagged fluctuations between action potentials compared to those observed in $h1$. Figure 7b shows the forward-in-time and backward-in-time cross-correlation functions between $V$ and $h1$. The black line represents the correlation function proceeding forward in time — denoted as $C_{Vh1}$, while the blue line corresponds to the function reverse in time — denoted as $C_{h1V}$. The lines exhibit an approximate phase-complementary periodic oscillation and gradually diminish in amplitude toward zero. Figure 7c illustrates the time-evolving trend of the difference between forward-in-time and backward-in-time cross-correlation functions — denoted as $C_{Vh1} - C_{h1V}$. Similarly, there are displayed periodic-like oscillations, with the amplitude gradually decreasing towards zero. It is important to
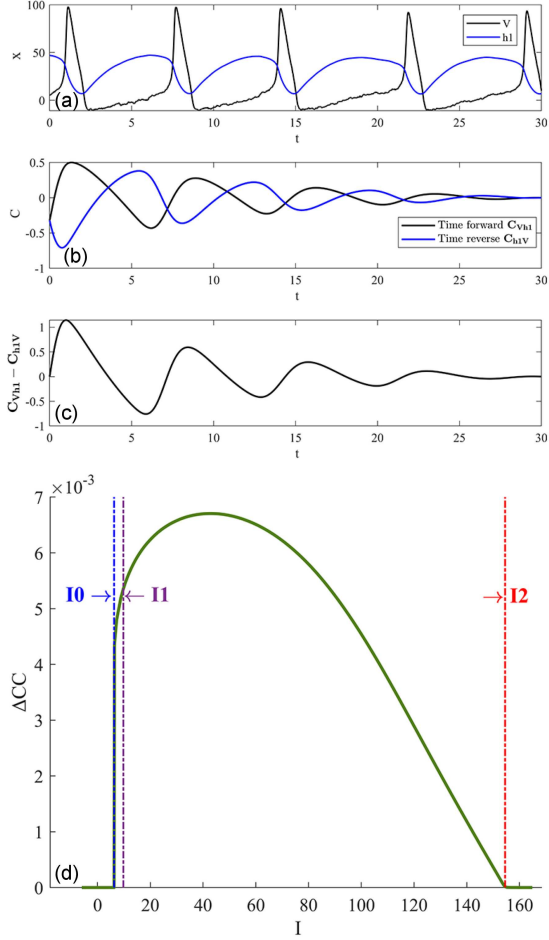
Fig. 7. Quatification of the time irreversibility and the degree of detailed balance breaking. (a) Trajectories of the membrane potential $V$ and $h1$ ($I = 10 \ \mu\mathrm{A/cm}^2$, $\mathcal{D} = 0.04$, and $h1 = 100h$). (b) Time-forward $C_{Vh1}$ (black) and time-reverse $C_{h1V}$ (blue) cross-correlation function between $V$ and $h1$. Panel (c) represents the difference between forward-in-time and backward-in-time cross-correlation functions, $C_{Vh1} - C_{h1V}$, plotted vs $t$. (d) Illustration of the average difference of $C_{Vh1} - C_{h1V}$, denoted as $\Delta CC$, in relation to $I$. The solid green line indicates the change in $\Delta CC$ vs the bifurcation parameter $I$. The purple vertical dashed line corresponds to the current $I_1$ at the first Hopf bifurcation point, H1, while the red vertical dashed line represents $I_2$ at the second Hopf bifurcation point, H2. The dark blue vertical dashed line corresponds to the current $I_0$.

note that in panels (a), (b), and (c), the condition $t = 0$ does not represent the initial time of recording the trajectory. Instead, it signifies a point in time reached after the system has been running for a sufficiently long time to attain a statistically steady state.

Figure 7d displays the variation of the average difference $C_{Vh1} - C_{h1V}$, denoted as $\Delta CC$, with respect to the bifurcation parameter $I$. The two
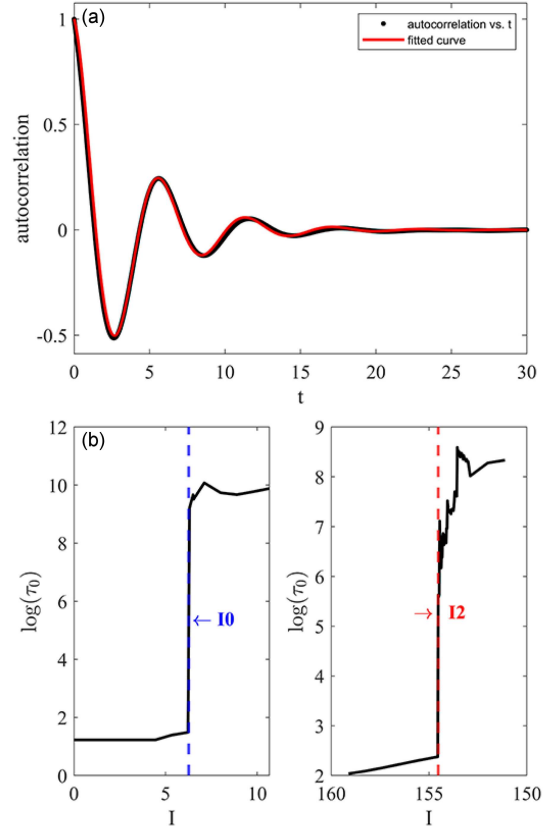


Fig. 8. The phenomenon of critical slowing down near the subcritical Hopf bifurcation point H1 in the Hodgkin–Huxley neuron. (a) The two-point autocorrelation function of $h1$ and its fitting line ($\mathcal{D} = 0.045$ and $I = 5.4709 \ \mu\mathrm{A/cm}^2$). (b) The natural logarithm of $\tau_0$ vs $I$ (black solid line). The dark blue dashed vertical line is $I_0 = 6.2645 \ \mu\mathrm{A/cm}^2$. The red dashed vertical line is $I_2 = 154.5266 \ \mu\mathrm{A/cm}^2$.

dashed lines represent the stimulus currents $I_1$ and $I_2$ corresponding to the two Hopf bifurcation points. The forward-in-time and backward-in-time cross-correlation functions serve as quantifiable indicators of detailed balance breaking and time irreversibility, respectively. Their experimental application, such as in the use of fluorescence correlation spectroscopy in single-molecule enzymology [44, 45], may be a practical method for identifying potential bifurcations or non-equilibrium phase transitions in HH neurons. Comparing this with Fig. 6, $\Delta CC$ exhibits a similar overall trend to $J_{av}$ and EPR, however, it shows an earlier significant change near $I_0$. This aligns with the boundary between the MPI and B regions in the deterministic bifurcation diagram (Fig. 1a), suggesting that $\Delta CC$ might be a more effective predictor of phase transitions compared to $J_{av}$ and EPR.

For neurons capable of transitioning from a resting state to spike firing, it is theoretically possible to provide an indicator regarding the characteristics of the critical slowing down as the neuron

approaches the first Hopf bifurcation point H1 from its resting state, as well as the H2 Hopf bifurcation point from the resting state. To observe the phenomenon of the critical slowing down within a finite observation window, we require appropriate noise intensity and an observation interval sufficiently close to H1 and H2. Adjusting these factors can enhance the accuracy and visibility of observing neuronal state transitions. We set $\mathcal{D} = 0.045$ and $\boldsymbol{A_\Gamma} = [1.0, 0.0001, 1.0, 0.0001]$ for our investigation. We used MATLAB to compute and normalize $h1$'s two-point autocorrelation function. Then, we applied the "cftool" toolbox to fit the resulting curve using the function $\exp(-x/\tau_0)\cos(wx)$, $w = 2\pi T$, where $\tau_0$ represents a coherence time for the oscillation [26, 46, 47]. Figure 8a illustrates the curve of autocorrelation function for $I = 5.4709\ \mu\text{A/cm}^2$. The red line signifies the fitted curve, which displays the remarkable proximity to the original data. Through this fitting process, we determined the value of $\tau_0$. In Fig. 8b, we plotted the natural logarithm of $\tau_0$ vs the current $I$. The natural logarithm of $\tau_0$ exhibits a dramatic change at $I_0$ and $I_2$, indicating a strong correlation between critical slowing down and Hopf bifurcation for the classical HH neuron model. Therefore, critical slowing down, average flux, EPR, and irreversible cross-correlation can provide indicators for bifurcation from the fluctuation, dynamics, thermodynamics, and time asymmetry perspectives.

## 4. Conclusions

In this study, we thoroughly investigated the local bistability properties of the original four-dimensional Hodgkin–Huxley equations under the influence of noise. Combined with landscape and flux theory, we conducted a comprehensive analysis of the stochastic dynamics of a single HH neuron, revealing the characteristics of potential landscapes and non-zero curl flux after it reaches a statistically steady state. We decomposed the driving force of the system into two parts: one closely related to the gradient of the probability distribution potential $U$, in short as the gradient force, and the other associated with the steady-state probabilistic flux $\boldsymbol{J_{ss}}$ and the steady-state probability distribution density $P_{ss}$. The gradient force tends to drag the real-time system state toward states with a larger probability distribution, effectively stabilizing the system state on stable attractors in non-equilibrium systems. The component associated with the steady-state probabilistic flux $\boldsymbol{J_{ss}}$, exhibiting a rotational characteristics, is dedicated to driving and sustaining periodic oscillations.

We explored how strong noise triggers oscillations prematurely, leading to a competitive coexistence between neuronal quiescence and spike discharges. Despite sufficient noise, the dominating rotational force driving the emergence and sustenance of stable oscillations dominates over the gradient force. Moreover, by evaluating the barrier height in co-existence states, we quantified the stability of the resting state and further investigated the stability of limit cycles in regions exclusively characterized by stable periodic oscillations.

Through computation of the entropy production rate (EPR) and the average probabilistic flux $J_{av}$, we discovered that both $J_{av}$ and EPR serve as quantitative indicators for bifurcations or phase transitions in the HH neurons. As it is not easy to directly measure these two metrics in experiments, we further discussed the average difference between forward-in-time and backward-in-time cross-correlations and the critical slowing down, which can be directly measured in experiments. Moreover, the average difference between forward-in-time and backward-in-time cross-correlations tends to undergo a break earlier than EPR and $J_{av}$, marking it as an earlier warning signal for bifurcation or phase transition points. In the original HH model, there exists a subcritical Hopf bifurcation rather than a saddle-node bifurcation, and the critical slowing down is closely associated with the subcritical Hopf bifurcation.

## Acknowledgments

## Appendix

### A1. The classical Hodgkin–Huxley equations and the Jacobian matrix in their deterministic form

The deterministic Hodgkin–Huxley model can be written as

$$C_m\frac{\mathrm{d}V}{\mathrm{d}t} = -\overline{g_\text{K}}n^4(V - V_\text{K}) - \overline{g_\text{Na}}m^3h(V - V_\text{Na})$$
$$-g_L(V - V_L) + I,$$

$$\frac{\mathrm{d}m}{\mathrm{d}t} = \alpha_m(V)(1 - m) - \beta_m(V)m,$$

$$\frac{\mathrm{d}h}{\mathrm{d}t} = \alpha_h(V)(1 - h) - \beta_h(V)h,$$

$$\frac{\mathrm{d}n}{\mathrm{d}t} = \alpha_n(V)(1 - n) - \beta_n(V)n. \qquad (9)$$

During the linear stability analysis, stochastic forces of the system are neglected and all equations on the left-hand side are set to zero. The corresponding

expressions on the right-hand side are denoted in order as $f_1, f_2, f_3, f_4$. Then, the Jacobian matrix in the deterministic form is as follows

$$\mathcal{J}_{Jacobi} = \begin{bmatrix} \frac{\partial f_1}{\partial V} & \frac{\partial f_1}{\partial m} & \frac{\partial f_1}{\partial h} & \frac{\partial f_1}{\partial n} \\ \frac{\partial f_2}{\partial V} & \frac{\partial f_2}{\partial m} & \frac{\partial f_2}{\partial h} & \frac{\partial f_2}{\partial n} \\ \frac{\partial f_3}{\partial V} & \frac{\partial f_3}{\partial m} & \frac{\partial f_3}{\partial h} & \frac{\partial f_3}{\partial n} \\ \frac{\partial f_4}{\partial V} & \frac{\partial f_4}{\partial m} & \frac{\partial f_4}{\partial h} & \frac{\partial f_4}{\partial n} \end{bmatrix} \tag{10}$$

Next, let us illustrate the procedure using $\frac{\partial f_2}{\partial V}$ and $\frac{\partial f_2}{\partial m}$ as examples. The remaining terms can be derived by similar methods, i.e.,

$$\frac{\partial f_2}{\partial V} = \frac{\partial}{\partial V}\big[\alpha_m(V)(1-m) - \beta_m(V)m\big] =$$

$$\frac{\partial}{\partial V}\big[\alpha_m(V) - m\alpha_m(V) - \beta_m(V)m\big] =$$

$$\dot{\alpha}_m(V) - [\dot{\alpha}_m(V)+\dot{\beta}_m(V)]m =$$

$$\dot{\alpha}_m(V)[\dot{\alpha}_m(V)+\dot{\beta}_m(V)]\frac{\alpha_m(V)}{\alpha_m(V)+\beta_m(V)} =$$

$$\big[\alpha_m(V)+\beta_m(V)\big]\left[\frac{\dot{\alpha}_m(V)[\alpha_m(V)+\beta_m(V)]}{[\alpha_m(V)+\beta_m(V)]^2}\right.$$

$$\left. -\frac{\alpha_m(V)[\dot{\alpha}_m(V)+\dot{\beta}_m(V)]}{[\alpha_m(V)+\beta_m(V)]^2}\right] = \lambda_m \dot{m}_\infty \frac{\partial f_2}{\partial m} =$$

$$-[\alpha_m(V)+\beta_m(V)] = -\lambda_m \tag{11}$$

In the above equations, $\lambda_m = \alpha_m(V) + \beta_m(V)$ and $m_\infty = \frac{\alpha_m(V)}{\alpha_m(V)+\beta_m(V)}$. The same procedure can be applied to derive other elements of the Jacobian matrices.

## A2. From Langevin equations (LEs) to Fokker–Planck equations

The system dynamics satisfy the following equation

$$\frac{dx_i}{dt} = f_i(\boldsymbol{x}, t) + \sum_{j=1}^{m} g_{ij}\Gamma_i(t). \tag{12}$$

The first two moments of the Langevin force component $\Gamma_i(t)$ are given by

$$\langle \Gamma_i(t) \rangle = 0,$$

$$\langle \Gamma_i(t_1)\Gamma_j(t_2) \rangle = 2\mathcal{D}_i\,\delta_{ij}\delta(t_1 - t_2), \tag{13}$$

where $i, j = 1, 2, ..., n$. The multiplication factor $g_{ij}$ in (12) eliminates the variations of stochastic forces to the variable $\boldsymbol{x}$. In (13), $\delta_{ij}$ satisfies

$$\delta_{ij} = \begin{cases} 1, & \text{if } i = j, \\ 0, & \text{if } i \neq j. \end{cases} \tag{14}$$

To deduce an equation satisfied by the system's distribution function $P(\boldsymbol{x}, t)$ from the Langevin equation (LE), it is essential to compute the various order transition moments $M_n(\boldsymbol{x}, t, \tau)$. As an example, we consider the one-dimensional case

$$M_n(x, t, \tau) = \langle \big(x(t+\tau) - x(t)\big)^n \rangle \quad (\tau \ll 1). \tag{15}$$

Starting from (12), the stochastic dynamics can be described by $\frac{dx}{dt} = f(x,t) + g(x,t)\Gamma(t)$. From here, it is easy to get

$$x(t+\tau)-x(t) = \int_t^{t+\tau} dt'\,\big[f(x(t'),t')+g(x(t'),t')\Gamma(t')\big]. \tag{16}$$

Assuming that the integrands $f$ and $g$ can be expanded in terms of $x(t')-x(t)$, it holds

$$f(x(t'),t')=f(x(t),t')+f'(x(t),t')(x(t')-x(t)) + \dots$$

$$g(x(t'),t')=g(x(t),t')+g'(x(t),t')(x(t')-x(t)) + \dots \tag{17}$$

Substituting the expression (17) into (16) yields

$$x(t + \tau) - x(t) = \int_t^{t+\tau} dt'\, f(x(t),t')$$

$$+ \int_t^{t+\tau} dt'\, f'(x(t),t')\big(x(t')-x(t)\big) + \dots$$

$$+ \int_t^{t+\tau} dt'\, g(x(t),t')\Gamma(t')$$

$$+ \int_t^{t+\tau} dt'\, g'(x(t),t')\big(x(t')-x(t)\big)\Gamma(t') + \dots \tag{18}$$

Repeatedly using (18) for the $x(t + \tau) - x(t)$ term in the expression gives

$$x(t + \tau)-x(t) = \int_t^{t+\tau} dt'\, f(x(t),t')$$

$$+ \int_t^{t+\tau} dt'\, f'(x(t),t') \int_t^{t'} dt''\, h(x(t'),t'')$$

$$+ \int_t^{t+\tau} dt'\, f'(x(t),t') \int_t^{t'} dt''\, \mu(x(t'),t'')\Gamma(t'')$$

$$+ \cdots + \int_t^{t+\tau} dt'\, g'(x(t),t')\Gamma(t')$$

$$+ \int_t^{t+\tau} dt'\, g'(x(t),t')\Gamma(t') \int_t^{t'} dt''\, h(x(t'),t'')$$

$$+ \int_t^{t+\tau} dt'\, g'(x(t),t')\Gamma(t') \int_t^{t'} dt''\, \mu(x(t'),t'')\Gamma(t'')$$

$$+ \dots \tag{19}$$

To understand the statistical properties of $x(t)$ and obtain higher-order correlations such as $\langle x(t_1)x(t_2)x(t_3)x(t_4)\dots \rangle$, we make the practical assumption that the random variable $\Gamma(t)$ follows a Gaussian distribution. That means,

$$\langle \Gamma(t_1)\Gamma(t_2)\Gamma(t_3)\dots\Gamma(t_{2n-1}) \rangle = 0,$$

$$\langle \Gamma(t_1)\Gamma(t_2)\Gamma(t_3)\dots\Gamma(t_{2n}) \rangle =$$

$$(2\mathcal{D})^n \sum_i^n [\delta(t_{i_1}-t_{i_2})\delta(t_{i_3}-t_{i_4})\dots\delta(t_{i_{2n-1}}-t_{i_{2n}})]. \tag{20}$$

By combining the statistical properties of the Langevin force mentioned above by (13) and (20) with (19), we can calculate the higher-order transition moments (see (15)). The first-order transition moment is given by

$$M_1(x,t,\tau) = \langle x(t+\tau) - x(t) \rangle =$$

$$\left[ f(x,t) + \mathcal{D}g'(x,t)g(x,t) \right]\tau + \mathcal{O}(\tau^2). \tag{21}$$

Here, $O(\tau^2)$ represents the higher-order infinitesimal of $\tau$. Similarly, one can obtain

$$M_2(x,t,\tau) = \langle [x(t+\tau) - x(t)]^2 \rangle =$$

$$2\mathcal{D}g^2(x,t)\tau + O(\tau^2), \tag{22}$$

and

$$M_n(x,t,\tau) = \langle [x(t+\tau) - x(t)]^n \rangle \le O(\tau^2) \tag{23}$$

for $n \ge 3$. Assuming that the process under investigation is a Markov process, and using $\rho(x,t)$ to represent its distribution function and $p$ to represent the probability of being in a certain state, the following relations are derived

$$\rho(x, t+\tau) = \int dx' \, p(x, t+\tau|x',t)\rho(x',t), \tag{24}$$

$$\rho(x, t+\tau) - \rho(x,t) = \frac{\partial \rho(x,t)}{\partial t}\tau + O(\tau^2). \tag{25}$$

In $p(x, t+\tau|x',t) = \int dy \, \delta(y-x)\, p(y, t+\tau|x',t)$, let expand the term $\delta(y-x)$, namely

$$\delta(y-x) = \delta(x'-x+y-x') =$$

$$\sum_{n=0}^{\infty} \frac{(y-x')^n}{n!}\left( \frac{\partial}{\partial x} \right)^n \delta(x'-x). \tag{26}$$

After substituting it into the previous integral identity (24), we get the result

$$p(x, t+\tau|x',t) =$$

$$\left[ 1 + \sum_{n=1}^{\infty} \frac{1}{n!}\left( -\frac{\partial}{\partial x} \right)^n M_n(x',t,\tau) \right]\delta(x'-x), \tag{27}$$

where

$$M_n(x',t,\tau) = \int dy \, (y-x')^n p(y, t+\tau|x',t). \tag{28}$$

Substituting (27) into (24) and comparing with (25), one gets

$$\frac{\partial \rho(x,t)}{\partial t} = L_{KM}\, \rho(x,t), \tag{29}$$

$$L_{KM} = \sum_{n=1}^{\infty} \left( -\frac{\partial}{\partial x} \right)^n D_n(x,t), \tag{30}$$

$$D_n(x,t) = \lim_{\tau \to 0} \frac{M_n(x,t,\tau)}{n!\tau}. \tag{31}$$

Since $p(x,t|x',t)$ is the transition probability at time $t'$ with an initial distribution satisfying $\rho(x,t) = \delta(x-x')$, this transition probability also follows

$$\frac{\partial p(x,t|x',t)}{\partial t} = L_{KM}\, p(x,t|x',t). \tag{32}$$

This is the Kramers–Moyal forward equation. Comparing the high-order moment equation $M_n$ here with the previously defined one, it is easy to obtain

$$D_1(x,t) = f(x,t) + \mathcal{D}g'(x,t)g(x,t),$$

$$D_2(x,t) = \mathcal{D}g^2(x,t),$$

$$D_n(x,t) = 0, \quad (n \ge 3). \tag{33}$$

Thus, the Kramers–Moyal equation with truncation at the second order of partial derivatives is

$$\frac{\partial \rho(x,t)}{\partial t} = -\frac{\partial}{\partial x}\left[ f(x,t) + \mathcal{D}g'(x,t)g(x,t) \right]\rho(x,t)$$

$$+\mathcal{D} - \frac{\partial^2}{\partial^2 x}\left[ g^2(x,t)\rho(x,t) \right]. \tag{34}$$

This is the Fokker–Planck equation for a one-dimensional variable system.

The Fokker–Planck equation corresponding to the multi-variable Langevin equations can be derived using a similar approach, i.e.,

$$\frac{\partial \rho(\boldsymbol{x},t)}{\partial t} = -\sum_i \frac{\partial}{\partial x_i}\left[ D_i(\boldsymbol{x},t)\rho(\boldsymbol{x},t) \right]$$

$$+\sum_i \sum_j \frac{\partial^2}{\partial x_i \partial x_j}[D_{ij}(\boldsymbol{x},t)\rho(\boldsymbol{x},t)], \tag{35}$$

$$D_i(\mathbf{x},t) = \lim_{\tau \to 0} \frac{\langle x_i(t+\tau) - x_i \rangle}{\tau} =$$

$$f_i(\boldsymbol{x},t) + D\sum_k \sum_l g_{kl}\frac{\partial}{\partial x_k}g_{il}, \tag{36}$$

$$D_{ij}(\boldsymbol{x},t) = \lim_{\tau \to 0} \frac{\langle [x_i(t+\tau)-x_i][x_j(t+\tau)-x_j] \rangle}{\tau} =$$

$$D\sum_k g_{ik}gjk. \tag{37}$$

## References

[1] A.L. Hodgkin, A.F. Huxley, B. Katz, *J. Physiol.* **116**, 424 (1952).

[2] A.L. Hodgkin, A.F. Huxley, *J. Physiol.* **116**, 449 (1952).

[3] A.L. Hodgkin, A.F. Huxley, *J. Physiol.* **116**, 473 (1952).

[4] A.L. Hodgkin, A.F. Huxley, *J. Physiol.* **116**, 497 (1952).

[5] A.L. Hodgkin, A.F. Huxley, *J. Physiol.* **117**, 500 (1952).

[6] M. Piccolino, *Trends Neurosci.* **25**, 552 (2002).

[7] B. Hassard, *J. Theor. Biol.* **71**, 401 (1978).

[8] J. Rinzel, R.N. Miller, *Math. Biosci.* **49**, 27 (1980).

[9] K. Aihara, G. Matsumoto, *Biophys. J.* **41**, 87 (1983).

[10] J. Guckenheimer, J.S. Labouriau, *Bull. Math. Biol.* **55**, 937 (1993).

[11] H. Fukai, S. Doi, T. Nomura, S. Sato, *Biol. Cybern.* **82**, 215 (2000).

[12] P. Rowat, *Neural Comput.* **19**, 1215 (2007).

[13] I. Bashkirtseva, L. Ryashko, *Int. J. Bifurc. Chaos* **29**, 1950186 (2019).

[14] C. Meunier, I. Segev, *Trends Neurosci.* **25**, 558 (2002).

[15] J.H. Goldwyn, E. Shea-Brown, *PLoS Comput. Biol.* **7**, e1002247 (2011).

[16] E.V. Pankratova, A.V. Polovinkin, E. Mosekilde, *Eur. Phys. J. B Condens. Matter Complex Syst.* **45**, 391 (2005).

[17] T. Takahata, S. Tanabe, K. Pakdaman, *Biol. Cybern.* **86**, 403 (2002).

[18] M. Güler, *Neural Comput.* **25**, 2355 (2013).

[19] J. Wang, L. Xu, E. Wang, *Proc. Natl. Acad. Sci.* **105**, 12271 (2008).

[20] J. Wang, *Adv. Phys.* **64**, 1 (2015).

[21] X. Fang, K. Kruse, T. Lu, J. Wang, *Rev. Mod. Phys.* **91**, 045004 (2019).

[22] H. Yan, L. Zhao, L. Hu, X. Wang, E. Wang, J. Wang, *Proc. Natl. Acad. Sci.* **110**, E4185 (2013).

[23] H. Yan, K. Zhang, J. Wang, *Chinese Phys. B* **25**, 078702 (2016).

[24] C. Li, E. Wang, J. Wang, *Biophys. J.* **101**, 1335 (2011).

[25] L. Xu, D. Patterson, A.C. Staver, S.A. Levin, J. Wang, *Proc. Natl. Acad. Sci.* **118**, e2103779118 (2021).

[26] K. Zhang, J. Wang, *J. Phys. Chem. B* **122**, 5487 (2018).

[27] X. Wang, Y. Wu, L. Xu, J. Wang, *J. Chem. Phys.* **159**, 154105 (2023).

[28] H. Yan, F. Zhang, J. Wang, *Commun. Phys.* **6**, 110 (2023).

[29] L. Xu, D. Patterson, S.A. Levin, J. Wang, *Proc. Natl. Acad. Sci.* **120**, e2218663120 (2023).

[30] H.C. Tuckwell, J. Jost, *Physica A* **388**, 4115 (2009).

[31] V. Baysal, Z. Saraç, E. Yilmaz, *Nonlinear Dyn.* **97**, 1275 (2019).

[32] Q. Kang, B.-Y. Huang, M.-C. Zhou, *IEEE Trans. Cybern.* **46**, 2083 (2015).

[33] A.S. Pikovsky J. Kurths, *Phys. Rev. Lett.* **78**, 775 (1997).

[34] A.A. Faisal, L.P.J. Selen, D.M. Wolpert, *Nat. Rev. Neurosci.* **9**, 292 (2008).

[35] H. Risken, *The Fokker-Planck Equation*, Springer, Berlin 1996.

[36] W. Coffey, Y.P. Kalmykov, *The Langevin Equation: With Applications to Stochastic Problems in Physics, Chemistry and Electrical Engineering*, Vol. 27, World Scientific, 2012.

[37] L. Xu, J. Wang, *J. Phys. Chem. B* **124**, 2549 (2020).

[38] F. Zhang, L. Xu, K. Zhang, E. Wang, J. Wang, *J. Chem. Phys.* **137**, 065102 (2012).

[39] P. Dayan, L.F. Abbott, *Theoretical Neuroscience: Computational and Mathematical Modeling of Neural Systems*, MIT press, 2005.

[40] J. Wang, L. Chen, X. Fei, *Chaos, Solit. Fractals* **31**, 247 (2007).

[41] S. Wiggins, *Introduction to Applied Nonlinear Dynamical Systems and Chaos*, Springer-Verlag, 2003.

[42] R.J. Sacker, *J. Differ. Equ. Appl.* **15**, 753 (2009).

[43] T. Tateno, A. Harsch, H.P.C. Robinson, *J. Neurophysiol.* **92**, 2283 (2004).

[44] H. Qian E.L. Elson, *Proc. Natl. Acad. Sci.* **101**, 2828 (2004).

[45] Q. Liu, J. Wang, *Proc. Natl. Acad. Sci.* **117**, 923 (2020).

[46] C. Meisel, A. Klaus, C. Kuehn, D. Plenz, *PLoS Comput. Biol.* **11**, e1004097 (2015).

[47] D.A. Steyn-Ross, M.L. Steyn-Ross, M.T. Wilson, J.W. Sleigh, *Phys. Rev. E* **74**, 051920 (2006).